

Development of the dense plasma focus for short-pulse applications

N. Bennett, M. Blasco, K. Breeding, D. Constantino, A. DeYoung, V. DiPuccio, J. Friedman, B. Gall, S. Gardner, J. Gatling, E. C. Hagen, A. Luttmann, B. T. Meehan, M. Misch, S. Molnar, G. Morgan, R. O'Brien, L. Robbins, R. Rundberg, N. Sipe, D. R. Welch, and V. Yuan

Citation: *Phys. Plasmas* **24**, 012702 (2017); doi: 10.1063/1.4973227

View online: <http://dx.doi.org/10.1063/1.4973227>

View Table of Contents: <http://aip.scitation.org/toc/php/24/1>

Published by the [American Institute of Physics](#)

Articles you may be interested in

Erratum: "Envelope equation for the linear and nonlinear propagation of an electron plasma wave, including the effects of Landau damping, trapping, plasma inhomogeneity, and the change in the state of wave" [*Phys. Plasmas* **23**, 102105 (2016)]

Phys. Plasmas **24**, 019901019901 (2017); 10.1063/1.4973832

Trapping and acceleration of hollow electron and positron bunch in a quasi-linear donut wakefield

Phys. Plasmas **24**, 013107013107 (2017); 10.1063/1.4973598

Scattering cross sections of the particles in the partially ionized dense nonideal plasmas

Phys. Plasmas **24**, 012101012101 (2017); 10.1063/1.4973324

Kinetic modeling of Langmuir probe characteristics in a laboratory plasma near a conducting body

Phys. Plasmas **24**, 012901012901 (2017); 10.1063/1.4972879

Development of the dense plasma focus for short-pulse applications

N. Bennett,¹ M. Blasco,¹ K. Breeding,¹ D. Constantino,¹ A. DeYoung,² V. DiPuccio,¹ J. Friedman,¹ B. Gall,¹ S. Gardner,¹ J. Gatling,¹ E. C. Hagen,¹ A. Luttmann,¹ B. T. Meehan,¹ M. Misch,¹ S. Molnar,¹ G. Morgan,² R. O'Brien,¹ L. Robbins,¹ R. Rundberg,² N. Sipe,¹ D. R. Welch,³ and V. Yuan²

¹National Security Technologies, LLC, Las Vegas, Nevada 89193, USA

²Los Alamos National Laboratory, Los Alamos, New Mexico 87545, USA

³Voss Scientific, LLC, Albuquerque, New Mexico 87108, USA

(Received 9 November 2016; accepted 13 December 2016; published online 5 January 2017)

The dense plasma focus (DPF) has long been considered a compact source for pulsed neutrons and has traditionally been optimized for the total neutron yield. In this paper, we describe the efforts to optimize the DPF for short-pulse applications by introducing a reentrant cathode at the end of the coaxial plasma gun. The resulting neutron pulse widths are reduced by an average of $21 \pm 9\%$ from the traditional long-drift DPF design. Pulse widths and yields achieved from deuterium-tritium fusion at 2 MA are 61.8 ± 30.7 ns FWHM and $1.84 \pm 0.49 \times 10^{12}$ neutrons per shot. Simulations were conducted concurrently to elucidate the DPF operation and confirm the role of the reentrant cathode. A hybrid fluid-kinetic particle-in-cell modeling capability demonstrates correct sheath velocities, plasma instabilities, and fusion yield rates. Consistent with previous findings that the DPF is dominated by beam-target fusion from superthermal ions, we estimate that the thermonuclear contribution is at the 1% level. *Published by AIP Publishing.*

[<http://dx.doi.org/10.1063/1.4973227>]

I. INTRODUCTION

The dense plasma focus (DPF) device has long been considered a compact source for pulsed neutron and x-ray generation^{1–3} and has provided an inexpensive platform for exploring plasma physics.^{4–7} With stored energies ranging from tens of joules to MJ,^{6,8} the DPF is being explored for a wide range of applications from activation analysis and plasma nanotechnology to radiography and material detection.^{9–13}

The DPF device derives from a coaxial plasma gun that is filled with a low-pressure deuterium and tritium gas mixture to generate significant fusion reactions as the plasma compresses. Development of the DPF has traditionally focused on maximizing the total fusion neutron yield,^{14–16} with more recent designs intended to increase portability and pulse repetition rates.^{17–20} In this report, we describe the first efforts to constrain the neutron pulse duration while retaining as much of the total yield as possible. This initial effort focuses on very modest variations on the Mather-type DPF hardware design, specifically the shape of the downstream electrode terminations, without changing the discharge times of the capacitor banks ($4 - 7 \mu\text{s}$) or the gas constituents.

The shorter neutron pulses are achieved using an anode center conductor with a blunt termination and reducing the plasma drift length to the downstream cathode to a value that is comparable to the coaxial gap width. We present here the first experiments comparing the performance of this design to the more traditional long drift chamber, which were conducted on two MA-scale DPF systems. The measured neutron yields and the pulse shapes are interpreted with the aid of hybrid fluid-kinetic particle-in-cell (PIC) simulations of the full DPF system. The simulations show that the MA-scale DPF operates in a regime in which neutron production

is dominated by the beam-target process, as expected,^{3,21} but with a pinching plasma that is tightly magnetically confined to the axis, achieving ion densities greater than 10^{21} cm^{-3} . The simulations provide supporting evidence that the thermonuclear component of the total neutron yield is approximately 1%.

To provide context for our modified electrode terminations, the physics of DPF operation, with the traditional long drift chamber, is presented in Sec. II. The modified drift chamber, referred to as a reentrant cathode, is described in Sec. III along with the diagnostics used in the experiments which compare its performance to the traditional DPF design. The decrease in the average pulse width achieved with the reentrant cathode is demonstrated in Sec. IV. Finally, the hybrid simulation technique, described in Sec. V, provides insight into the plasma dynamics of the DPF, the role of the new hardware, and the beam-target nature of the fusion reactions.

II. PHYSICS OF THE DPF Z PINCH

The DPF device is a coaxial accelerator with a blunt anode termination that is filled with a low-density gas, typically deuterium (labeled “DD” for the interacting ions) or a deuterium-tritium (DT) mixture. As the accelerator is pulsed, the gas is ionized and accelerated through the $\mathbf{j} \times \mathbf{B}$ force to the end of the anode. The plasma pinches at the anode tip with sufficient velocity to create neutrons by fusion processes.

DPF operation is categorized into four phases, depicted in Fig. 1. The gas ionizes in the first phase with the arrival of a high-voltage pulse. The conductivity increases rapidly as the current-carrying plasma sheath is formed. As the current

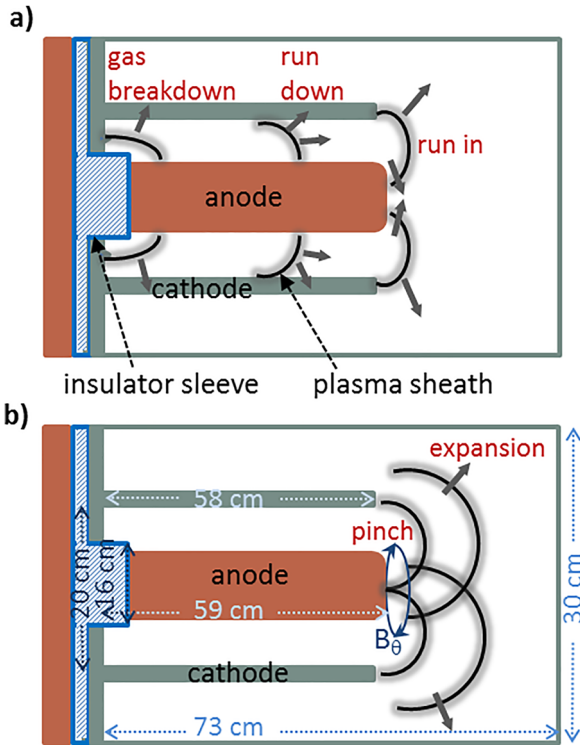


FIG. 1. The DPF operation is illustrated in five phases. During *gas-breakdown*, the voltage pulse is injected through the insulator sleeve (blue) and a plasma sheath (black) is formed between the anode tube (orange) and the cylindrical cathode (green). This sheath is accelerated axially during *run-down* and radially during *run-in*. After the *pinch*, the plasma expands radially and axially to the outer cathode. The dimensions shown are for the experiments reported in this paper.

rises and the $\mathbf{j} \times \mathbf{B}$ force increases, the plasma sheath is accelerated to the end of the anode. This second phase is referred to as *run-down*. The third phase, or *run-in*, occurs after the plasma sheath reaches the end of the anode and is accelerated radially inward. In the *pinch* phase, the plasma densities and temperatures (energies) have increased sufficiently to enable fusion reactions.

The relevant fusion processes for the DPF are beam-target and thermonuclear, which are distinguished by the plasma ion energy and density distributions. To determine the thermonuclear contribution, the fusion reaction rate $n_1 n_2 \langle \sigma v \rangle$ is calculated assuming Maxwellian distributions for the ion densities n_i and relative velocity v . The calculated thermonuclear yield falls significantly below the measured rate in DPF devices, therefore the remainder must be accounted for by the beam-target fusion from the non-Maxwellian tails of the ion energy distributions.^{22–25} The high levels of nonthermal (beam) ions collide with the lower energy (target) ions, resulting in high DPF yields. The high energy ions are accelerated by unexpectedly high electric field gradients from instabilities in the pinch region.^{25,26}

Previous research has concluded that beam-target dominates for peak currents less than ~ 2 MA,²¹ while the thermonuclear yield overtakes beam-target as the peak current increases until dominating at approximately 18 MA.²⁷ Kinetic simulations of deuterium Z-pinchs have shown that between 7 and 15 MA, half of the neutrons generated are thermonuclear and half are beam-target.²⁵ Therefore, the

experiments and simulations discussed in this report, with pinch currents of 2 – 2.5 MA, are expected to be dominated by beam-target fusion.

III. DPF EXPERIMENTAL SETUP AND DIAGNOSTICS

The experiments presented here were conducted on two DPF systems, both with peak currents in the range 2 – 2.5 MA.²⁸ One of the DPF systems is operated exclusively with DD gas and is driven by four 432 μF modules operated as two parallel Marx banks storing 1.1 MJ at peak charge. The second device is capable of operating with DD or DT gas and is driven by a 576 μF capacitor bank storing 350 kJ at full charge. Both devices were operated between 32 and 35 kV with common DPF hardware configurations as illustrated in Fig. 1 for the traditional DPF with a blunt anode and Fig. 2 with the addition of the reentrant cathode.

In both configurations, the anode extends 59.4 cm into the gas cell and is surrounded by a 58-cm-long cathode formed by a concentric array of 24 knife-edge rods. The anode outer radius is 7.62 cm and the cathode inner radius is 10.16 cm. The reentrant cathode shown in Fig. 2 is the same diameter as the anode and extends from the cathode end-plate to within 4.5 cm of the anode.

The purpose of the reentrant cathode is to limit the fusion reaction time by reducing the axial region over which pinching occurs. (It may also be used to house small targets, thereby locating them closer to the pinch region and increasing the incident neutron fluence.) The design is motivated by time-resolved images of plasma optical emission during pinch, such as shown in Fig. 3, which shows an axial progression of the plasma away from the anode. This axial motion, referred to as *zippering*, is expected from plasma-gun-type devices and is seen in time-resolved images in Refs. 3, 29, 30, and 31. A similar cathode modification was

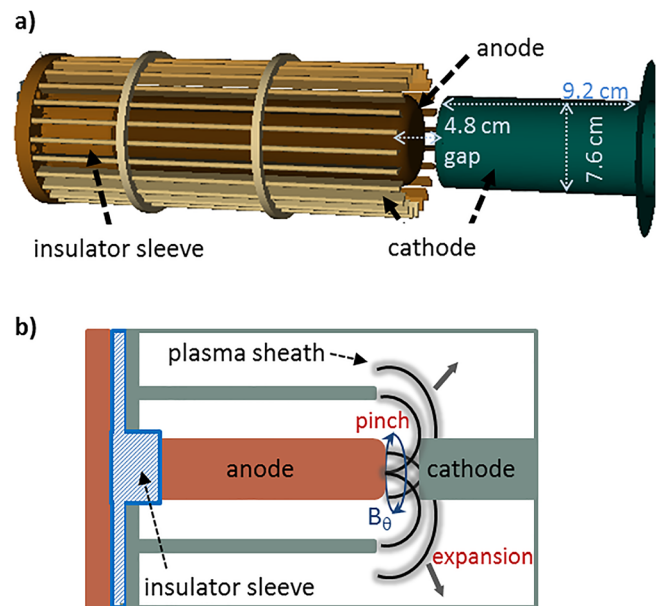


FIG. 2. (a) Illustration of the DPF hardware with a radiused anode tube and the optional reentrant cathode. (b) The pinch and plasma expansion phases of DPF operation are constrained axially with the inclusion of the reentrant cathode.

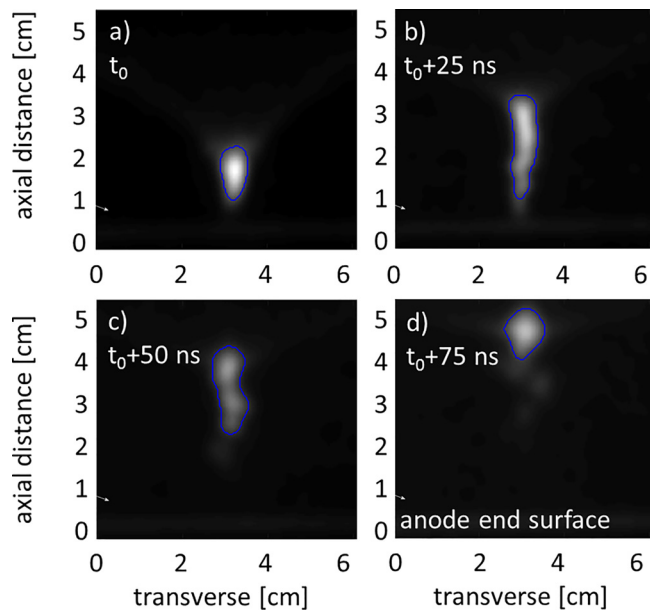


FIG. 3. Optical emission during the pinch phase from DD fusion reactions during a single shot, using the four-432- μ F-module bank at 35 kV and 3 Torr. The images have a 5-ns exposure and 25-ns separation and were gated during the pinch phase. The image is smoothed with a Gaussian filter (3σ in an 11×11 window). The optical pinch is extracted using the k-means clustering algorithm.³³

reported in Ref. 32, but with the aims of increasing the energy density and creating an electrode configuration more similar to larger Z-pinch machines.

The primary diagnostics for this study are time-resolved and integrated neutron measurements. The total neutron yield is measured using the foil-activation technique with different target materials for DD and DT neutrons based on energy thresholds.^{34–37} For each shot, the yield is obtained in minutes using activation counter units comprised of a thin foil, scintillator, and photomultiplier tube (PMT). The activation isotopes in the thin foil must, therefore, have half-lives measured in seconds to minutes. This technique is calibrated daily against a yield measured using a high-efficiency counting chamber. This second technique requires activation isotopes with half-lives of several minutes to allow time to transport the target material from the experiment to the counting chamber.

For detecting DT neutrons (14.1 MeV), ^{141}Pr is the preferred material because the threshold for $^{141}\text{Pr} + n \rightarrow ^{140}\text{Pr} + 2n$ is above 10 MeV, and it is highly insensitive to γ radiation, which virtually eliminates background.³⁷ For detecting DD neutrons (2.45 MeV), beryllium has become a primary target material because its 1-MeV threshold for $^9\text{Be} + n \rightarrow ^6\text{He} + \alpha$ eliminates background from scattered neutrons. In addition, the reaction cross section is peaked near 2.5 MeV, providing discrimination between DD and DT neutrons.

Details regarding the characterization and calibration of the yield detectors are found in Refs. 28 and 38. To minimize the measurement uncertainty for the yields, the entire high-efficiency counting chamber systems were calibrated at Sandia National Laboratories' Ion Beam Laboratory. The total measurement uncertainty for the source calibration and cross-calibration method is 6% for ^{141}Pr and 9% for ^9Be .

Neutron pulse shapes are recorded using scintillator-PMT detector assemblies surrounded by lead shielding to reduce the photon background.³⁸ (The PMT impulse responses are 2.5–3.0 ns and the scintillating material is specified to have a 0.35-ns rise and 1.6-ns decay.) Two detectors with different scintillator material are fielded for redundancy. Both are mounted 30 cm from the DPF pinch in the radial direction. Neutron time-of-flight is measured 10 m from the pinch using a matched pair of scintillator-PMT detectors. One detector is shielded from the line-of-sight of the pinch by a neutron shadow-bar composed of stacked tungsten and polyethylene cylinders, and thus records the scattered background only. The neutron signal is the subtraction of the shielded detector from the unshielded detector.

IV. MEASURED NEUTRON YIELDS AND PULSE SHAPES

Representative pulses delivered by the traditional DPF configuration (Fig. 1) are plotted in Fig. 4. These pulses were recorded sequentially for a fixed bank voltage and deuterium gas pressure using a scintillator-PMT detector located 30 cm from the pinch. The variation in pulse shapes in Fig. 4 appears consistent with observations of multiple peaks in the neutron pulses from other experiments. For example, two peaks were observed in Ref. 39, and three peaks were observed in the neutron pulses in Refs. 40 and 31, with resulting pulse full-width at half-maximum (FWHM) values >200 ns.

The long tails in the neutron pulses plotted in Fig. 4 are enabled by the long drift chamber in which the plasma may continue to weakly pinch as it is transported axially and the energetic ions slow down. This tail is reduced with the use of the reentrant cathode, as shown in the representative pulses in Fig. 5. On average, the pulse FWHM values are reduced with the reentrant cathode by $21 \pm 9\%$. The uncertainty in this average is dominated by the wide distribution of pulse widths generated by the traditional DPF, as shown in Fig. 6. The FWHM distribution from the reentrant cathode is seen in Fig. 6 to occupy the low end of the range for the traditional DPF. Therefore, the reduction in the average width is simply achieved by depopulating the high-value tail of the traditional distribution. This is consistent with previous observations of an axially propagating plasma and successive pinch necking produced by $m = 0$ instabilities.^{3,41}

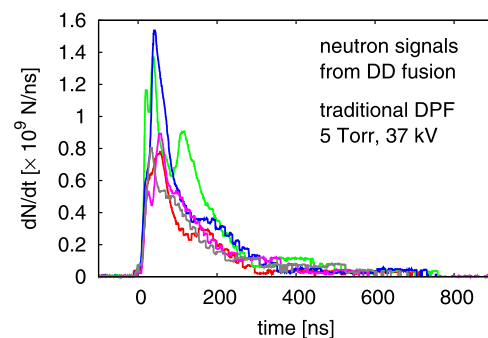


FIG. 4. Measured neutron pulse shapes obtained from sequential shots in the standard DPF configuration in Fig. 1 with a 59-cm-long anode tube. The data were collected on the four-432- μ F-module bank at 37 kV charge and with DD gas pressure of 5 Torr.

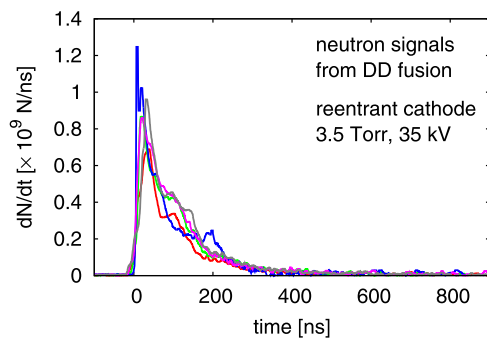


FIG. 5. Measured neutron pulse shapes using the reentrant cathode (Fig. 2) and a 59-cm-long anode tube. The data were collected on the four-432- μ F-module bank at 35 kV charge and with the DD gas pressure of 3.5 Torr.

The reduced pulse widths correspond to lower integrated neutron yields. The average and standard deviation of the DD neutron yield for the traditional DPF shots in Fig. 6 is $2.79 \pm 1.34 \times 10^{11}$. Measurement uncertainty contributes an additional $\pm 9\%$. With the reentrant cathode, the yield is $2.05 \pm 0.81 \times 10^{11}$ neutrons per shot.

An experimental series of 117 shots was conducted using the reentrant cathode with a DT gas mixture on the 576- μ F capacitor bank. Sample pulse shapes are plotted in Fig. 7. The distributions of pulse FWHM and yields for these shots are plotted in Fig. 8. The average FWHM is 61.8 ± 30.7 ns with $1.84 \pm 0.49 \times 10^{12}$ neutrons per shot. Measurement uncertainty contributes an additional $\pm 6\%$ for the yield and could reduce the pulse width by as much as 5 ns.

The expectation that the pinch duration is reduced by limiting the plasma drift time is supported by hybrid PIC simulations which include the run-down and run-in phases. The simulations described in Sec. V were conducted for both the traditional DPF configuration and the reentrant cathode.

V. SIMULATION TECHNIQUE AND VALIDATION

A comprehensive model of the DPF device is challenging given the μ s time scales required to ionize the gas and

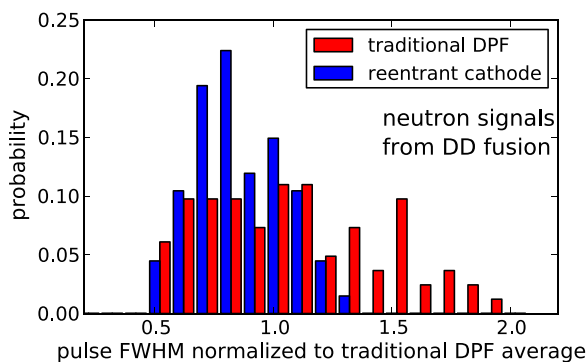


FIG. 6. The distribution of the measured neutron pulse FWHM for the reentrant cathode configuration (Fig. 2) compared to the traditional configuration (Fig. 1) from DD fusion. The data were collected on the four-432- μ F-module bank at 35 kV charge and with a gas pressure range of 3.5 to 5.5 Torr. The statistics in the normalized distributions are 82 shots for the traditional DPF and 67 for the reentrant cathode. Relative pulse widths are provided because these signals were recorded using the shadow-bar system 10 m from the pinch and, therefore, includes the time-of-flight spreading.

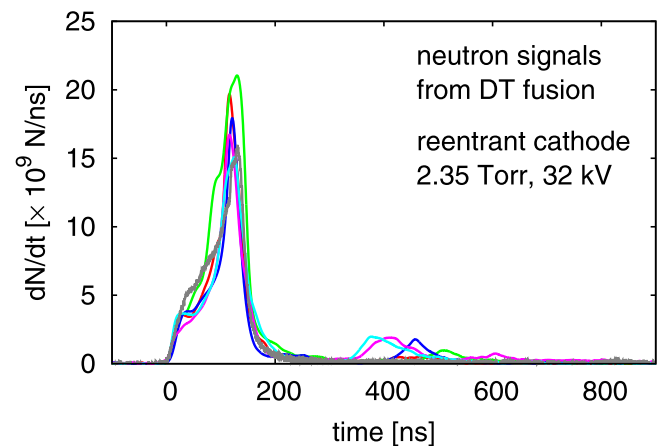


FIG. 7. Measured neutron pulse shapes using the reentrant cathode (Fig. 2) and a 59-cm-long anode tube. The data were collected on the 576 μ F bank at 32 kV charge and with a DT gas pressure of 2.35 Torr.

transport the plasma down the anode, the high plasma densities achieved as the plasma pinches, the dominance of kinetic effects in beam-target fusion, and the presence of instabilities. Traditionally magnetohydrodynamic (MHD) codes have been used to model the run-down phase of the DPF, but are not able to reproduce the observed neutron yields.^{42,43} Particle-in-cell (PIC) codes can treat particles kinetically, allowing for binary collisions and charge separation that are essential to reproducing the pinch physics, but require spatial

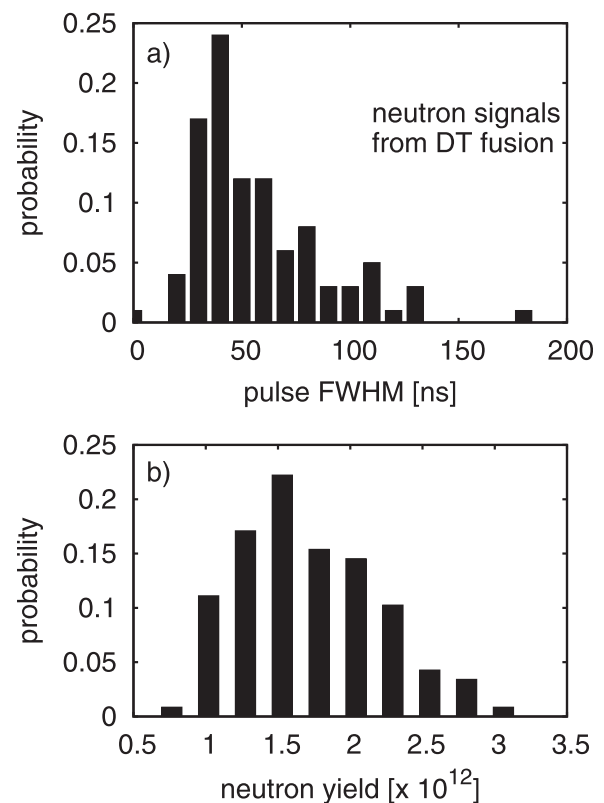


FIG. 8. The distributions of the measured neutron pulse FWHM (a) and yield (b) for the reentrant cathode configuration in Fig. 2 from DT fusion. The average FWHM is 61.8 ± 30.7 ns with $1.84 \pm 0.49 \times 10^{12}$ neutrons per shot. The operating conditions are 32 kV at 2.27–3.25 Torr or 33 kV at 2.45–2.8 Torr on the 576- μ F capacitor bank. The gas mixture was composed of 53.7% tritium.

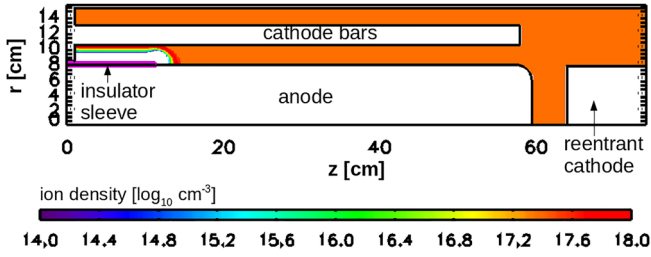


FIG. 9. Simulation geometry for the DPF with a reentrant cathode in 2D cylindrical coordinates (r, z). Pulsed power is injected through the Pyrex insulator sleeve (shown in pink). The deuterium ion density is shown at 1.6 μs into the pulse for a 35-kV bank charge at 5.5 Torr.

resolution near 100 μm and correspondingly small time steps.^{44,45} Nonetheless, by limiting the simulated volume to the pinch region, recent PIC simulations of a 180-kA DPF have successfully reproduced the measured neutron yield,²⁶ ion energy distributions, and electric field oscillations.⁷

Simulations of the MA-scale DPF presented here are performed using the fully relativistic electromagnetic particle-in-cell code CHICAGO, from the developers of LSP.^{46–49} A hybrid fluid/kinetic treatment⁵⁰ was developed to reduce computation times and has enabled simulations of the entire DPF tube and driving circuit. The plasma is modeled as a

quasi-neutral, Eulerian fluid during the run-down and run-in phases, after which the particles are transitioned to a kinetic treatment for the pinch.

The quasi-neutral fluid treatment relaxes constraints on the timestep by using the MHD assumption of zero charge density, or $n_e \sim Z_i n_i$, where n_e and n_i are the electron and ion number densities, Z_i is the ion charge state. Therefore, it is possible to follow an ion kinetic macroparticle that carries the fluid information for the inertia-less electrons.⁵¹ The equation of motion for the composite ion-electron macroparticle is

$$m_i n_i \frac{d\mathbf{v}}{dt} = \mathbf{j} \times \mathbf{B} - \nabla(p_e + p_i), \quad (1)$$

where p_e and p_i are the electron and ion pressures, and assuming zero viscosity. The current is

$$\mathbf{j}_{ohms} = \sigma \left(\mathbf{E} + \mathbf{v}^* \times \mathbf{B} - \frac{\nabla p_e}{en_e} \right), \quad (2)$$

where \mathbf{v}^* is the drift velocity and the conductivity, $\sigma = e^2 n_e / \nu_m$, is calculated using the Lee-More-Desjarlais model⁵² for the collision rate. Equations (1) and (2) are advanced assuming Maxwellian distributions for n_i and temperature in each grid cell.

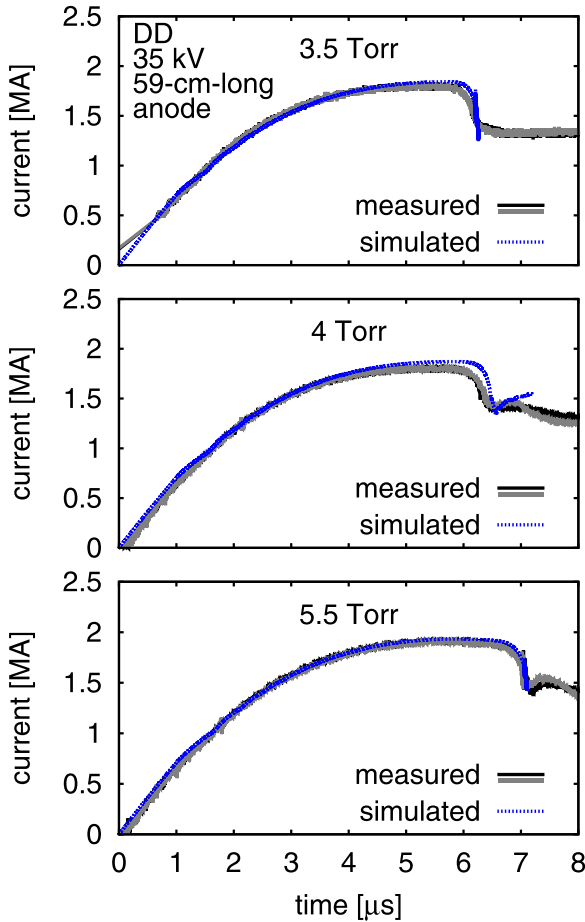


FIG. 10. The simulated currents (blue) are compared to measurement (grey and black) for the reentrant cathode hardware configuration (59-cm-long anode tube). The bank voltage is 35 kV for DD gas pressures of (a) 3.5 Torr, (b) 4 Torr, and (c) 5.5 Torr. Two measured currents are shown at each gas pressure.

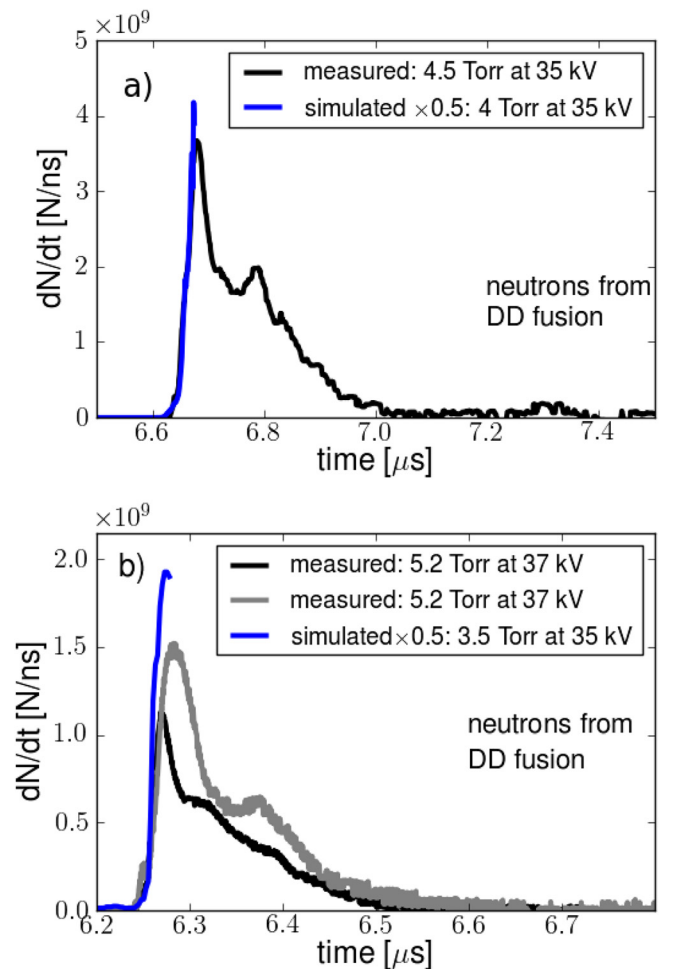


FIG. 11. Simulated neutron pulses from DD fusion (blue) are compared to measurement (black and grey) for (a) the traditional DPF configuration and (b) the reentrant cathode. The simulated pulses are scaled by 0.5.

The particles are transitioned to a kinetic treatment during the run-in phase, just before their collision rates becomes insufficient to maintain the Maxwellian distributions. A single fluid particle is transitioned to thousands of electron and ion particles per cell in a manner that conserves the momentum and charge. These kinetic particles are then advanced via their individual momenta, binary collision frequencies, and fusion interactions, with no assumed distributions.

The simulations presented here are initialized with deuterium plasma. All DD and DT fusion reactions are modeled, and the resulting proton, tritium, ^3He , and neutron particles are treated kinetically. The simulations are conducted in 2D cylindrical coordinates (r, z) with the geometry as shown in Fig. 9. As compared to the hardware illustration in Fig. 2, the simulations assume azimuthal symmetry and include the entire gas-filled chamber. The resolution in the pinch region ($0 < r < 2.0$ cm and $59.0 < z < 64.0$ cm) is $100 \mu\text{m}$ and $200 \mu\text{m}$ in the radial and axial directions, respectively. The plasma motion through the cathode bars is approximated in 2D using a transparency model by which a prescribed fraction of incident particles are absorbed. Simulations were conducted for the traditional DPF configuration and with the reentrant cathode.

To use the hybrid technique, we must assume that the fill gas is initially fully ionized. Preliminary models of the gas-breakdown phase indicate that breakdown occurs within $1 \mu\text{s}$, before the plasma sheath undergoes significant $\mathbf{j} \times \mathbf{B}$ acceleration (for a capacitor bank discharge time of $4 - 7 \mu\text{s}$). The accuracy of the simulations with respect to

the bank circuit, fluid model, and tube geometry is verified in comparison to measured currents, shown in Fig. 10. In the three examples shown, the voltage is held constant while the deuterium gas pressure is varied from 3.5 to 5.5 Torr. The simulated run-down times are within 4% of the measured values. Simulations of different tube geometries show a similar agreement with the data.

The transition to the kinetic particle treatment occurs during the inductively driven drop in current in Fig. 10, after which the simulations progress much more slowly. Initial results for the pinch phase have been obtained for simulations of the traditional DPF configuration and the reentrant cathode. The progress of these simulations is indicated in Fig. 11, in which the incomplete simulated neutron pulses are compared to data. In both cases, the simulated yield rate is roughly a factor of two larger than data. This may be attributed to the ideal pinch conditions generated in the 2D simulations.

VI. PLASMA DYNAMICS DURING RUN-IN AND PINCH

The hybrid simulations provide an insight into the measured run-down times, run-in plasma sheath perturbations, and neutron yields. During run-down, the $\mathbf{j} \times \mathbf{B}$ force exerted on the plasma sheath is resisted by the pressure of the neutral gas in its path, resulting in the initial sheath velocities inversely proportional to the gas density. As the sheath moves downstream, incorporating more of the DPF tube length into the current path, the equivalent circuit inductance increases as $L(z) = (\mu/2\pi)\ln(r_c/r_a)z$, causing j^2 to decrease.

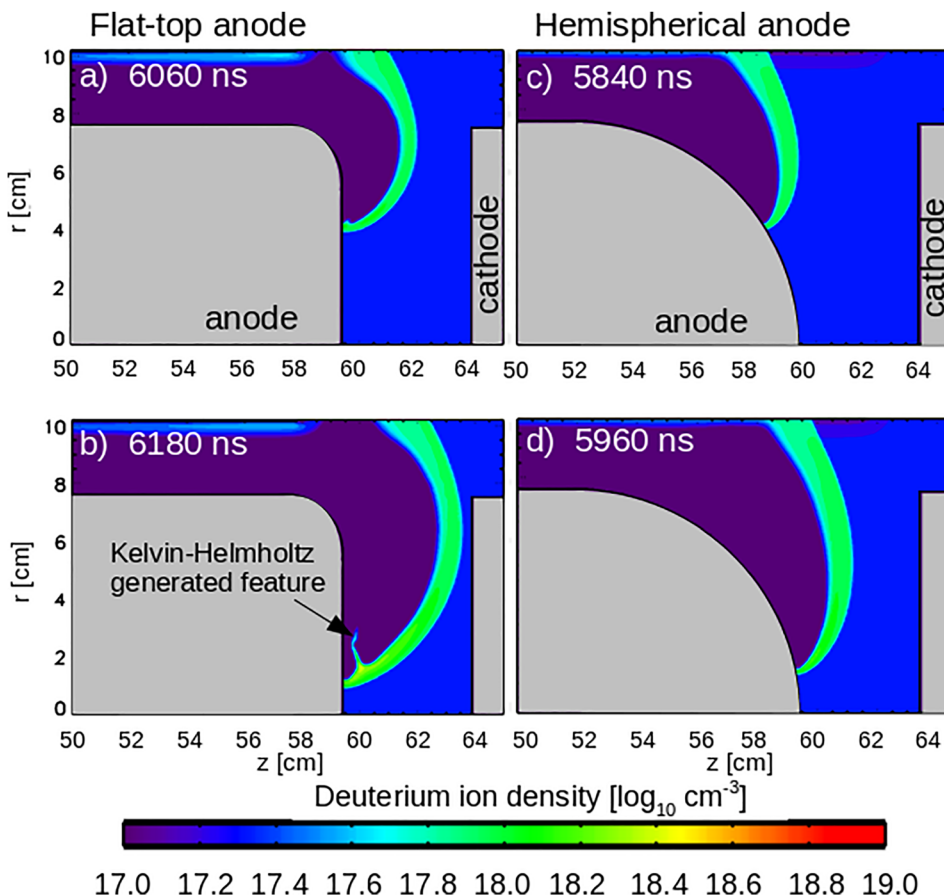


FIG. 12. Simulated ion density contours during run-in for the flat-top (top) and hemispherical (bottom) anodes. The contours show the region at the end of the anode only, which occupy $0 < r < 10.0$ cm and $50.0 < z < 65.0$ cm in Fig. 9. The densities for the flat-top anode shown in (a) and (b) are separated by 120 ns. The densities for the hemispherical anode shown in (c) and (d) are also separated by 120 ns. Although the initial conditions for both simulations are a 35-kV bank charge and 3.5-Torr gas pressure, the plasma reaches the axis sooner with the hemispherical anode due to its shape.

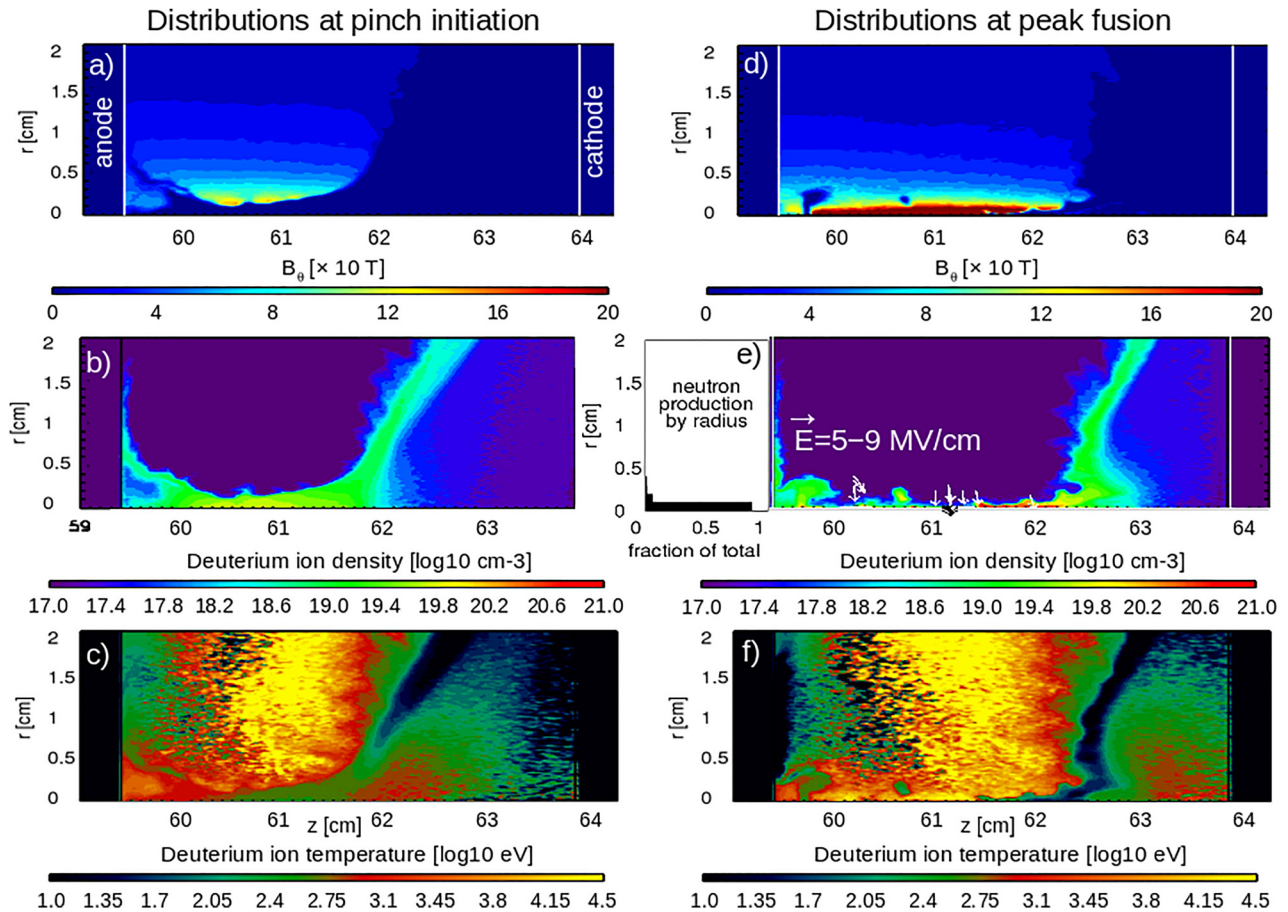


FIG. 13. Simulated contour maps of B_θ (top), deuterium ion density (middle), and deuterium ion temperature (bottom) during the pinch phase from the simulation geometry shown in Fig. 9 (zoomed in to $0 < r < 2.0$ cm and $59.0 < z < 64.3$ cm.) The distributions at 6238 ns after bank discharge are plotted in (a) through (c) while the distributions at 6258 ns are plotted in (d) through (f). The radial distribution of neutron production is plotted to the left of (e) and the vector for electric field stresses greater than 5 MV/cm are overlaid. The bank voltage of 35 kV and the DD gas pressure of 3.5 Torr (for the Fig. 9 tube dimensions) result in the pinch initiating 6205 ns after bank discharge.

(Here z is the axial location of the plasma sheath, r_c is the cathode inner radius, and r_a is the anode outer radius.) Thus the force is reduced on the initially faster, lower-density gas fills, so that the run-down times are not exactly inversely proportional to the density, as indicated in Fig. 10.

The density distribution of the plasma sheath during run-in is influenced by the anode shape. The flat-top anode of Fig. 1 elongates the sheath as it transitions to run-in and enhances the velocity shear, which drives the Kelvin-Helmholtz instability. This is shown in the plasma density contours in Figs. 12(a) and 12(b), which show two snapshots

of the plasma during run-in, zoomed into the region at the end of the anode. (For reference, this region is $0 < r < 10.0$ cm and $50.0 < z < 65.0$ cm in Fig. 9). By contrast, the plasma density contours generated by an anode with a hemispherical termination are seen in Figs. 12(c) and 12(d) to remain more radial in structure during the pinch and be less susceptible to this instability.

A design more prone to instabilities would exhibit larger variations in output, such as the wide pulse width distribution shown in Fig. 6. However, instabilities, especially in the $m = 0$ mode, are desirable in the DPF because they have

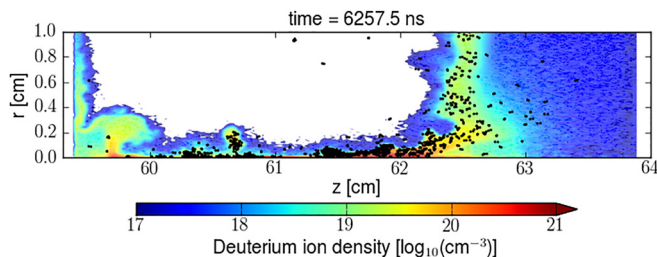


FIG. 14. A simulated ion density contour map is overlaid with a scatter plot of neutron creation locations, depicted as black dots. The neutrons are generated primarily via $DD \rightarrow n + {}^3\text{He}$, although the chain $DD \rightarrow p + T$ followed by $DT \rightarrow n + {}^4\text{He}$ is enabled. The full simulation geometry is shown in Fig. 9, and zoomed in here to $0 < r < 1.0$ cm and $59.0 < z < 64.0$ cm.

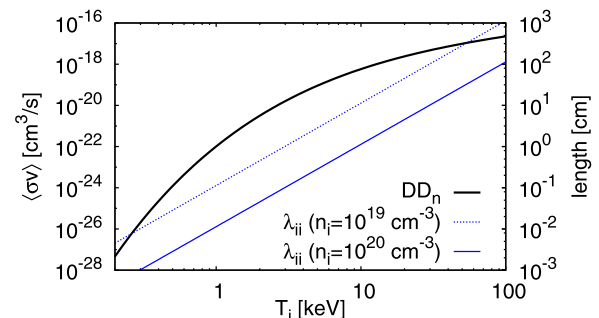


FIG. 15. The $DD \rightarrow n + {}^3\text{He}$ reactivity⁵⁴ and deuterium ion mean-free-path (λ_{ii}) as functions of T_i .

been shown to increase the beam-target fusion yields.^{3,40,50,53} Both conclusions are supported by measurements taken on the 1.1-MJ DPF showing more consistent pulse widths but lower yields with a round-top anode. Specifically, at 35 kV and 5.5-Torr DD gas pressure, the total neutron yield for the flat-top anode with reentrant cathode is $2.05 \pm 0.81 \times 10^{11}$, while the yield from the hemispherical anode is approximately half this value.

The $m = 0$ -type instabilities increase neutron yield in the beam-target regime by enhancing ion beam energies. Previous work has shown that such instabilities increase the local electric field stresses which accelerate ions between regions of high density.^{25,53} The simulations performed here for 2-MA pinches support this. The results for the reentrant cathode are used to illustrate the formation of high-density targets and lower-density, higher-temperature regions in which the electric field stresses reach the MV/cm levels. Figure 13 shows the deuterium ion density, temperature ($T_i = \frac{2}{3} \langle E_i \rangle / k$), and azimuthal magnetic field (B_θ) in the region between the anode and the reentrant cathode ($0 < r < 2.0$ cm and $59.0 < z < 64.3$ cm in Fig. 9) at two times, first during initial plasma compression and again during peak neutron production. Pockets of high-density plasma are confined to $r < 1$ mm for tens of ns during the pinch under the influence of magnetic fields of order 100 T. The mean T_i in the high-density regions is approximately 400 eV, while the less-constrained ions reach tens of keV. Electric fields in the low-density regions are not uniformly axial, but may be directed radially inward as shown in Fig. 13(e). We note that these 2D simulations represent a more idealized pinch than would be achieved in 3D.

While Fig. 13(e) shows that neutrons are generated within a mm of the axis, Fig. 14 provides a more detailed 2D map of neutron production. While neutron creation is correlated with regions of high plasma density ($> 10^{19}$ cm⁻³), few are created in the high-density region near the anode. This is consistent with ion acceleration away from the anode toward downstream target regions and provides further confirmation that the DPF is dominated by beam-target fusion from superthermal ions.²²⁻²⁵

Figure 13 may be used to estimate the ratio of beam-target to thermonuclear fusion. The mean T_i in the high-density regions corresponds to a reactivity of 10^{-25} cm³/s, as shown in Fig. 15. Using $n_i \sim 10^{21}$ cm⁻³ within a volume of ~ 0.001 cm³, from Fig. 14, the thermonuclear rate for the highest density regions is $\sim 10^5$ N/ns. If the volume is broadened to include $r \leq 1$ mm, the ion energy distribution within this region is plotted in Fig. 16. The peak of the energy distribution fits to a 1.1-keV Maxwellian and the average density in this region is $\sim 10^{20}$ cm⁻³. The corresponding reactivity, 10^{-22} cm³/s, provides an estimate of the thermonuclear contribution to the total yield rate of $\sim 10^7$ N/ns. Estimating from Fig. 16 that ions above 100 keV are 10^{-4} of the total and that they impact target ions in the high-density regions, the reactivity and the yield rate for beam-target fusion are $\sim 10^{-17}$ cm³/s and $\sim 10^9$ N/ns, respectively. This is consistent with the measured yield rate in Fig. 11, which reaches 1.5×10^9 N/ns. A crude estimate of the thermonuclear fusion contribution in a 2-MA pinch is approximately 1%.

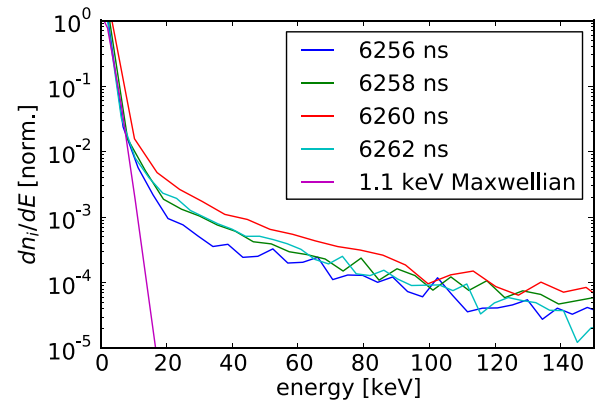


FIG. 16. The kinetic energy distribution of deuterium ions during the pinch from the simulation geometry is shown in Fig. 9. The peak is fit to a 1.1-keV Maxwellian.

While the beam-target dominates in the MJ-class DPF, it is distinguished somewhat from lower energy devices in that the plasma is more collisional during the pinch. The deuterium ion mean free path (λ_{ii}) from the collision frequency (ν_i)⁵⁵ is

$$\lambda_{ii} = \frac{2\pi\epsilon_0^2 m_i^2 v_i^4}{Z_i^4 e^4 \ln \Lambda n_i},$$

where v_i is the ion velocity, and $\ln \Lambda$ is the Coulomb logarithm. Expressed in terms of kinetic energy, λ_{ii} is shown as a function of T_i in Fig. 15 for two representative values of n_i chosen from Fig. 13. The lower temperature ions found in the high-density regions are highly collisional, so the aggregate energy spectrum in Fig. 16 is closer to a Maxwellian than that measured for a 1.2-kJ DPF.⁷

VII. SUMMARY

The DPF device is a compact source for intense neutron pulses that has traditionally been optimized for the total neutron yield. We have implemented a modest change to the Mather-type device in order to develop the DPF for short-pulse applications. In the modified DPF design, a reentrant cathode replaces the long-drift chamber at the end of the DPF coaxial plasma gun. This reentrant cathode reduces the plasma drift length to a value comparable to the coaxial gap width.

The neutron pulses generated in a traditional DPF may have long tails and be of relatively long (hundreds of ns) duration because the plasma may continue to weakly pinch as it is transported axially. By limiting the drift time, the reentrant cathode operates in the low range of achievable pulse widths. The results are reduced neutron pulse tails and the FWHM values are reduced by an average of $21 \pm 9\%$ from the traditional DPF design. Pulse widths and yields achieved from the deuterium-tritium fusion at 2 MA are 61.8 ± 30.7 ns FWHM and $1.84 \pm 0.49 \times 10^{12}$ neutrons per shot.

Simulations were conducted concurrently to elucidate the DPF operation and confirm the role of the reentrant cathode. A hybrid fluid-kinetic particle-in-cell modeling capability demonstrates correct sheath velocities, plasma instabilities, and fusion

yield rates. Consistent with previous findings that the DPF is dominated by beam-target fusion from superthermal ions,^{22–25} we estimate that the thermonuclear contribution is at the 1% level.

ACKNOWLEDGMENTS

The authors thank Dr. Daniel Marks and Dr. Mark Kiefer for reviewing this work.

This manuscript has been authored by the National Security Technologies, LLC, under Contract No. DE-AC52-06NA25946 with the U.S. Department of Energy, National Nuclear Security Administration, Office of Defense Nuclear Nonproliferation Research and Development. The United States Government retains and the publisher, by accepting the article for publication, acknowledges that the United States Government retains a non-exclusive, paid-up, irrevocable, worldwide license to publish or reproduce the published form of this manuscript, or allow others to do so, for United States Government purposes. The U.S. Department of Energy will provide public access to these results of federally sponsored research in accordance with the DOE Public Access Plan (<http://energy.gov/downloads/doe-public-access-plan>) DOE/NV/25946–3065.

- ¹J. W. Mather, *Phys. Fluids* **7**, S28 (1964).
- ²J. W. Mather, *Phys. Fluids* **8**, 366 (1965).
- ³A. Bernard, P. Cloth, H. Conrads, A. Coudeville, G. Gourlan, A. Jolas, C. Maisonnier, and J. Rager, *Nucl. Instrum. Methods* **145**, 191 (1977).
- ⁴S. Lee and S. H. Saw, *Appl. Phys. Lett.* **92**, 021503 (2008).
- ⁵B. L. Bures and M. Krishnan, *Phys. Plasmas* **19**, 112702 (2012).
- ⁶E. Hagen, D. Lowe, R. O'Brien, S. Molnar, and B. Meehan, in *2013 Abstracts IEEE International Conference on Plasma Science (ICOPS)* (2013), p. 1.
- ⁷A. Schmidt, A. Link, D. Welch, J. Ellsworth, S. Falabella, and V. Tang, *Phys. Rev. E* **89**, 061101 (2014).
- ⁸L. Soto, *Plasma Phys. Controlled Fusion* **47**, A361 (2005).
- ⁹V. Gribov, A. Dubrovsky, L. Karpinski, R. Miklaszewski, M. Paduch, M. Scholz, P. Strzyewski, and K. Tomaszewski, *AIP Conf. Proc.* **875**, 415 (2006).
- ¹⁰T. Zhang, J. Lin, A. Patran, D. Wong, S. M. Hassan, S. Mahmood, T. White, T. L. Tan, S. V. Springham, S. Lee, P. Lee, and R. S. Rawat, *Plasma Sources Sci. Technol.* **16**, 250 (2007).
- ¹¹S. Hussain, S. Ahmad, M. Z. Khan, M. Zakaullah, and A. Waheed, *J. Fusion Energy* **22**, 195 (2003).
- ¹²M. Krishnan, *IEEE Trans. Plasma Sci.* **40**, 3189 (2012).
- ¹³R. S. Rawat, *IEEE Trans. Plasma Sci.* **41**, 701 (2013).
- ¹⁴F. N. Beg, M. Zakaullah, G. Murtaza, and M. M. Beg, *Phys. Scr.* **46**, 152 (1992).
- ¹⁵M. Zakaullah, A. Waheed, S. Ahmad, S. Zeb, and S. Hussain, *Plasma Sources Sci. Technol.* **12**, 443 (2003).
- ¹⁶R. Verma, P. Lee, S. Lee, S. V. Springham, T. L. Tan, R. S. Rawat, and M. Krishnan, *Appl. Phys. Lett.* **93**, 101501 (2008).
- ¹⁷S. Lee, P. Lee, G. Zhang, X. Feng, V. A. Gribov, M. Liu, A. Serban, and T. K. S. Wong, *IEEE Trans. Plasma Sci.* **26**, 1119 (1998).
- ¹⁸L. Rapezzi, M. Angelone, M. Pillon, M. Rapisarda, E. Rossi, M. Samuelli, and F. Mezzetti, *Plasma Sources Sci. Technol.* **13**, 272 (2004).
- ¹⁹R. Shukla, A. Shyam, R. Verma, E. Mishra, M. Meena, K. Sagar, and P. Dhang, *IEEE Trans. Plasma Sci.* **43**, 2354 (2015).
- ²⁰R. Niranjana, R. K. Rout, R. Srivastava, T. C. Kaushik, and S. C. Gupta, *Rev. Sci. Instrum.* **87**, 033504 (2016).
- ²¹D. Klir, J. Kravarik, P. Kubes, K. Rezac, S. Ananev, Y. Bakshaev, P. I. Blinov, A. Chernenko, E. Kazakov, V. D. Korolev, G. Ustrov, L. Juha, J. Krasa, and A. Velyhan, *IEEE Trans. Plasma Sci.* **37**, 425 (2009).
- ²²O. A. Anderson, W. R. Baker, S. A. Colgate, J. Ise, and R. V. Pyle, *Phys. Rev.* **110**, 1375 (1958).
- ²³W. Stygar, G. Gerdin, F. Venneri, and J. Mandrekas, *Nucl. Fusion* **22**, 1161 (1982).
- ²⁴P. Kubes, J. Kravarik, D. Klir, K. Rezac, M. Bohata, M. Scholz, M. Paduch, K. Tomaszewski, I. Ivanova-Stanik, L. Karpinski, and M. J. Sadowski, *IEEE Trans. Plasma Sci.* **37**, 83 (2009).
- ²⁵D. R. Welch, D. V. Rose, C. Thoma, R. E. Clark, C. B. Mostrom, W. A. Stygar, and R. J. Leeper, *Phys. Plasmas* **17**, 072702 (2010).
- ²⁶A. Schmidt, V. Tang, and D. Welch, *Phys. Rev. Lett.* **109**, 205003 (2012).
- ²⁷C. A. Coverdale, C. Deeney, A. L. Velikovich, J. Davis, R. W. Clark, Y. K. Chong, J. Chittenden, S. Chantrenne, C. L. Ruiz, G. W. Cooper, A. J. Nelson, J. Franklin, P. D. LePell, J. P. Apruzese, J. Levine, and J. Banister, *Phys. Plasmas* **14**, 056309 (2007).
- ²⁸N. Bennett, M. Blasco, K. Breeding, D. Constantino, A. DeYoung, V. DiPuccio, J. Friedman, B. Gall, S. Gardner, J. Gatling, E. Hagen, A. Luttmann, B. Meehan, M. Misch, S. Molnar, G. Morgan, R. O'Brien, L. Robbins, P. Ross, R. Rundberg, N. Sipe, and D. W. V. Yuan, "Development of the dense plasma focus as a short-pulse neutron source," Technical Report No. DOE/NV/25946-2970 (National Security Technologies, LLC, 2016).
- ²⁹J. M. Bayley, G. Decker, W. Kies, M. Mlzig, F. Miller, P. Rwekamp, J. Westheide, and Y. V. Sidelnikov, *J. Appl. Phys.* **69**, 613 (1991).
- ³⁰P. Kubes, J. Kravarik, D. Klir, K. Rezac, M. Scholz, M. Paduch, K. Tomaszewski, I. Ivanova-Stanik, B. Bienkowska, L. Karpinski, M. J. Sadowski, and H. Schmidt, *IEEE Trans. Plasma Sci.* **34**, 2349 (2006).
- ³¹P. Kubes, D. Klir, J. Kravarik, K. Rezac, E. Litseva, I. Ivanova-Stanik, L. Karpinski, M. Paduch, M. Scholz, H. Schmidt, and M. J. Sadowski, in *2007 16th IEEE International Pulsed Power Conference* (2007), Vol. 2, pp. 1699–1702.
- ³²P. Kubes, D. Klir, M. Paduch, T. Pisarczyk, M. Scholz, T. Chodukowski, Z. Kalinowska, K. Rezac, J. Kravarik, J. Hitschfel, J. Kortanek, B. Bienkowska, I. Ivanova-Stanik, L. Karpinski, M. J. Sadowski, K. Tomaszewski, and E. Zielinska, *IEEE Trans. Plasma Sci.* **40**, 1075 (2012).
- ³³S. Lloyd, *IEEE Trans. Inf. Theory* **28**, 129 (1982).
- ³⁴A. Judd, *Nucl. Instrum. Methods* **23**, 29 (1963).
- ³⁵O. Jarvis, E. Clipsham, M. Hone, B. Laundry, G. Sadler, P. van Belle, M. Pillon, M. Rapisarda, and K. Verschuur, *Fusion Technol.* **20**, 265 (1991).
- ³⁶C. W. Barnes, A. R. Larson, G. LeMunyan, and M. J. Loughlin, *Rev. Sci. Instrum.* **66**, 888 (1995).
- ³⁷T. Meehan, E. Hagen, C. Ruiz, and G. Cooper, *Nucl. Instrum. Methods Phys. Res., Sect. A* **620**, 397 (2010).
- ³⁸A. DeYoung, A. Hayes, J. Gorley, G. Morgan, V. Yuan, A. Obst, R. Rundberg, H. Li, G. Jungman, M. Snowball, M. Fowler, E. Guardincerii, S. Sterbenz, R. King, and N. King, "First NDSE LDRD proof-of-concept experiments," Technical Report No. LA-CP-16-20465 (Los Alamos National Laboratory, 2016).
- ³⁹V. A. Gribov, A. Banaszak, B. Bienkowska, A. V. Dubrovsky, I. Ivanova-Stanik, L. Jakubowski, L. Karpinski, R. A. Miklaszewski, M. Paduch, M. J. Sadowski, M. Scholz, A. Szydlowski, and K. Tomaszewski, *J. Phys. D: Appl. Phys.* **40**, 3592 (2007).
- ⁴⁰H. R. Yousefi, S. R. Mohanty, Y. Nakada, H. Ito, and K. Masugata, *Phys. Plasmas* **13**, 114506 (2006).
- ⁴¹F. Castillo, M. Milanese, R. Moroso, and J. Pouzo, *J. Phys. D: Appl. Phys.* **33**, 141 (2000).
- ⁴²D. Potter, *Phys. Fluids* **14**, 1911 (1971).
- ⁴³C. Kueny, D. Flicker, and D. Rose, "ALEGRA-HEDP simulations of the dense plasma focus," Technical Report No. sand2009-6373 (Sandia National Laboratories, 2009).
- ⁴⁴D. R. Welch, D. V. Rose, R. E. Clark, C. B. Mostrom, W. A. Stygar, and R. J. Leeper, *Phys. Rev. Lett.* **103**, 255002 (2009).
- ⁴⁵D. R. Welch, D. V. Rose, C. Thoma, R. E. Clark, C. B. Mostrom, W. A. Stygar, and R. J. Leeper, *Phys. Plasmas* **18**, 056303 (2011).
- ⁴⁶D. Welch, D. Rose, B. Oliver, and R. Clark, in *Proceedings of the 13th International Symposium on Heavy Ion Inertial Fusion [Nucl. Instrum. Methods Phys. Res., Sect. A* **464**, 134 (2001)].
- ⁴⁷D. R. Welch, D. V. Rose, R. E. Clark, T. C. Genoni, and T. P. Hughes, in *Proceedings of the 18th International Conference on the Numerical Simulation of Plasmas [Comput. Phys. Commun.* **164**, 183 (2004)].
- ⁴⁸D. Rose, D. Welch, B. Oliver, R. Clark, D. Johnson, J. Maenchen, P. Menge, C. Olson, and D. Rovang, *J. Appl. Phys.* **91**, 3328 (2002).
- ⁴⁹D. Welch, T. Genoni, R. Clark, and D. Rose, *J. Comput. Phys.* **227**, 143 (2007).

- ⁵⁰D. T. Offermann, D. R. Welch, D. V. Rose, C. Thoma, R. E. Clark, C. B. Mostrom, A. E. W. Schmidt, and A. J. Link, *Phys. Rev. Lett.* **116**, 195001 (2016).
- ⁵¹C. Thoma, D. R. Welch, and S. C. Hsu, *Phys. Plasmas* **20**, 082128 (2013).
- ⁵²M. Desjarlais, *Contrib. Plasma Phys.* **41**, 267 (2001).
- ⁵³A. Schmidt, A. Link, D. Welch, B. T. Meehan, V. Tang, C. Halvorson, M. May, and E. C. Hagen, *Phys. Plasmas* **21**, 102703 (2014).
- ⁵⁴H.-S. Bosch and G. Hale, *Nucl. Fusion* **32**, 611 (1992).
- ⁵⁵T. Boyd and J. Sanderson, *The Physics of Plasmas* (Cambridge University Press, 2003).